Materials Chemistry and Physics 237 (2019) 121838

Contents lists available at ScienceDirect

Materials Chemistry and Physics

journal homepage: www.elsevier.com/locate/matchemphys

Influence of copper on the structural, mechanical, and biological characteristics of Mg–1Al–Cu alloy

Narges Safari, Mohammad Reza Toroghinejad, Mahshid Kharaziha *

Department of Materials Engineering, Isfahan University of Technology, Isfahan, 84156-83111, Iran

HIGHLIGHTS

- Mg–Al–Cu alloys containing various Cu contents were developed via spark plasma sintering.
- Formation of Al_2Cu phase during SPS improved mechanical properties of Mg alloy.
- Mg–Al-0.25Cu alloys reduced degradation rate of pure Mg and Mg–1Al alloy.
- Mg–1Al-0.25Cu alloy promoted viability of MG63 compared to Mg–1Al alloy.
- Mg–Al–Cu significantly prevented from the growth of bacteria.

ARTICLE INFO

Keywords:
Magnesium alloy
Degradation rate
Mechanical property
Cytotoxicity
Antibacterial activity

ABSTRACT

The aim of this study was to develop biodegradable and antibacterial Mg–Al–Cu alloys consisting of various amounts of Cu content (0, 0.25, 0.5 and 1 wt%) using spark plasma sintering (SPS) approach. Moreover, the role of Cu on the physical and biological properties of the alloys was investigated. The results indicated the formation of Al_2Cu intermetallic phase during the SPS process significantly improved the mechanical properties of Mg based alloys. Specifically, the compressive strength and yield strength of pure Mg (167 ± 9 MPa and 69 ± 9 MPa, respectively) significantly enhanced to 232 ± 2 MPa and 94 ± 9 MPa, respectively, in Mg–1Al-0.25Cu alloy. Moreover, formation of tertiary alloy simultaneously improved the degradation rate, biocompatibility and antibacterial properties of pure Mg, depending on the Cu concentration. Noticeably, incorporation of 0.25 wt% Cu significantly diminished degradation rate from 0.039 cm/h in pure Mg to 0.00584 cm/h in Mg–1Al-0.25Cu alloy. Moreover, Mg–1Al-0.25Cu alloy noticeably promoted viability of MG63 cells compared to pure Mg, owing to the optimized ion release. The antibacterial activity results of samples against *Escherichia coli* and *Staphylococcus aureus* revealed that Mg–Al–Cu significantly prevented from the growth of bacteria, depending on the Cu content. In summary, Mg–Al-0.25Cu alloy with suitable mechanical characteristics, diminished degradation rate, good biocompatibility and antibacterial activities might be a promising biodegradable material for orthopedic implant.

1. Introduction

Millions of people in the world suffer from bone diseases such as arthritis, osteoporosis, bone fracture and tumor [1]. Between them, bone fractures, as the most common skeletal disorders, happen due to car accident, injuries in sports activities and aging [2]. Metallic based orthopedic implants have been widely applied to mechanically fix the damaged bone [3]. In order to provide successful bone treatment, bone fixtures should provide appropriate mechanical properties, near to those of bone tissue (compressive strength of 130–180 MPa, Young's modulus of 3–20 GPa and elongation of 10%) [4]. In another word, depending on the time of presentation in the human body, metallic implants are divided into two types of degradable or non-degradable (permanent implant) [5]. Based on the main concerns facing with the application of permanent metallic implants, including stress shielding and secondary surgical consequences, biodegradable implants have been developed [6–8]. Recently, Mg and its alloys with unique properties such as low density (1.74–2.0 gr/cm^3) and elastic modulus (41–45 GPa) near to those of bone tissue (1.8–2.1 gr/cm^3 and 3–20 GPa, respectively) are widely applied as a new group of degradable biomaterials for temporary

* Corresponding author.
E-mail address: kharaziha@cc.iut.ac.ir (M. Kharaziha).

https://doi.org/10.1016/j.matchemphys.2019.121838
Received 22 April 2019; Received in revised form 5 July 2019; Accepted 7 July 2019
Available online 9 July 2019

orthopedic implants [9–11]. In addition, magnesium is one of the critical elements in the human body and in various biological cycles. The amount of Mg is about 25 g in body of adult human with 70 kg weight. It needs to mention that more than half of the total amounts stored in bone tissue. Magnesium ions also activate many enzymes and stabilize the structures of DNA and RNA [12]. In addition, corrosion products of magnesium are not only non-toxic for human, but also could encourage new bone growth [13]. However, poor mechanical strength and corrosion properties of pure Mg result in development of various Mg based alloys [14]. Based on the effective role aluminum (Al) on the corrosion resistivity and mechanical properties of magnesium, Mg–Al alloys have been widely developed as implant materials [15]. However, the systematic cytotoxicity reported from Al ions results in the development of alloys with less Al elements (less than 1 wt%) [16].

The current and most important challenge facing with bone fixtures is irritation due to formation of biofilm [17]. During the implantation of bone fixtures, bacteria adhere to an implant surface leading to biofilm formation and consequent infection. Biofilms are resistant to the antibiotics, disinfectants, phagocytosis and inflammatory defense system of the body, which result in serious complications such as osteomyelitis with consequent devastating effects on bone and soft tissues around it [18]. To overcome this issue, various types of antibiotics such as Vancomycin [19] and Gentamicin [20] have been loaded in the implants. Another strategy to overcome the biofilm infection is formation of various antimicrobial coatings on the implant surface such as CuO-polydimethylsiloxane (PDMS) [21], chitosan based [22] and silver doped titania (TiO_2) thin film coatings [23]. Despite the promising results, these approaches show issues consisting of the requirement of additional steps for antibiotic loading, and antimicrobial coating as well as toxic side effects [24]. Therefore, scientists interested about the development of antimicrobial and degradable metallic implants consisting of antimicrobial metals including silver (Ag) [25], zinc (Zn) [26], and copper (Cu) [27]. Copper is a common antimicrobial metal which can confront with a wide range of microbes such as bacteria, fungi, algae and viruses [28]. Rashad et al. [29] developed Mg–Cu–Al alloy consisted of 1 wt% Cu using metallurgy powder technique and found that the mechanical properties of the alloy enhanced compared to Mg–Al alloy. However, degradation rate and antibacterial activity of this alloy were not investigated. In another study, Li et al. [27] developed Mg–Cu alloy and found that incorporation of 0.25 wt% copper in a Mg based implant could provide the appropriate antibacterial characteristics and good mechanical properties. In another study, Liu et al. [30] evaluated the mechanical, biological and antibacterial properties of Mg–Cu alloy with different amounts of Cu element (0.03, 0.19 and 0.57 wt%). They reported a good ultimate compressive strength in Mg-0.03Cu alloy (199.67 MPa) compared to pure Mg (185.67 MPa). Furthermore, the viability of MC3T3-E1 and HUVECs cells after incubation with Mg-0.03Cu and Mg-0.19Cu alloys enhanced compared to Mg-0.57Cu alloy. However, the role of various concentrations of Cu on the degradation rate of alloy was not investigated.

In order to develop magnesium based alloys, various strategies have been developed consisting of die-cast [31], ball-milling [32] and powder metallurgy [33]. Recently, powder metallurgy technique has been widely applied to produce Mg based alloys. Powder metallurgy is a comfortable approach to produce various alloys at low cost [34]. However, the common metallurgy powder process often faced with two main issues for Mg based alloys consisting of extensive oxidation and high reaction tendency [35]. Therefore, spark plasma sintering (SPS), a new advanced powder metallurgy method with high-speed of sintering has been introduced as a promising approach to produce active metal samples like magnesium based alloys [36]. In the SPS process, the surface of powder heated fast and metallic powders could be sintered in lower melting temperatures and a short time (10 min) in the vacuum condition. Consequently, the unique features of SPS approach consisting of fast heating, less oxidation at higher temperature, lower working temperatures than conventional sintering, and its shorter time process have resulted in the application of this approach for various metallic based alloys [37–40]. Based on our knowledge, the fabrication of Mg–Al–Cu alloy using SPS approach has not been investigated, yet.

In the present study, we used SPS approach to develop antibacterial and degradable Mg based alloy, consisting of various amounts of copper element (0.25, 0.5 and 1 wt%). It is expected that incorporation of both Al and Cu could simultaneously control mechanical properties, corrosion resistivity, antibacterial activity and cytotoxicity of Mg alloys making them suitable for bone fixtures.

2. Materials and methods

2.1. Materials

Magnesium powder (99.8% purity, Fe: ≤500 mg/kg, particle size less of 70 μm), aluminum powder (99.8% purity less of 60 μm particles size range) and copper powder (99.8% purity, particle size less of 63 μm) were supplied from Merck Co.

2.2. Fabrication of Mg–1Al-xCu alloy

Mg–1Al-xCu alloy was fabricated via a two-step mechanical alloying and SPS process, as schematically presented in Fig. 1. Before SPS process, Mg–Al–Cu powder mixtures consisting of different amounts of copper (0, 0.25, 0.5 and 1 wt%) were prepared. Primarily, Cu and Al powders consisting of various concentrations of Cu powder (0, 20, 33 and 50 wt %) were mixed using a high-energy ball milling (Retsch Pm100 model) with stainless steel containers and balls. The weight ratio of balls: powder was kept at 12:1. Moreover, 1 wt% stearic acid was added to the initial powders to prevent from the agglomeration of powders. Moreover, ball diameter (10 mm), milling times (20 h) and milling speed (200 rpm) were kept constant in whole experiment. After milling, the powders were distributed in ethanol with the concentration of 20 wt%, while magnetically stirred for 60 min. Consequently, Al-xCu suspensions (20 wt% in ethanol) were added to magnesium powder dispersed in ethanol with the concentration of 20 wt%, drop wisely. After 3 h mixing by mechanical agitator with the rate of 2000 (rpm), the temperature of the mixtures was enhanced to 70 °C to eliminate ethanol. The mixtures were finally dried in a vacuum oven (Teb Azma) at 70 °C for 2 h.

Homogeneous mixture of metal powders was consequently loaded into cylindrical graphite dies with 15 mm diameter and SPS machine (KPF, Model) was applied to densify the powders. SPS process parameters such as sintering temperature (600 °C), uniaxial pressure (40 MPa), processing time (10 min) and the heating and cooling rate (75 °C/min) were kept constant. Moreover, to prevent from oxidation process, sintering process was performed in a vacuum condition. In order to better evaluate the role of Cu element, Mg and Mg–Al bulks were similarly fabricated.

2.3. Characterizations of Mg–1Al-xCu alloy

The chemical composition of the samples was evaluated by X-ray diffraction (XRD, Phillips) with Cu Kα radiation. The crystallite size of milled powders was calculated using the Williamson-Hall method [41]. The phase transformation temperature was determined by differential thermal analysis (DTA, Linseis L70/2171) under argon atmosphere at a heating-cooling rate of 10 °C/min.

The microstructure of the samples was also studied by optical microscope (OM, digital Keyence VH-Z100) and scanning electron microscope (SEM, Philips, XL30) supplied with Oxford EDS system and X-ray mapping. Prior to microstructure analysis, all samples were grounded with SiC papers up to 5000 grit and polished with alumina suspensions. In order to evaluate the microstructure of surface and fracture surface of samples using optical microscope, they were etched in a solution of 100 μl acetic acid, 5 ml distilled water and 15 ml ethanol. Subsequently,

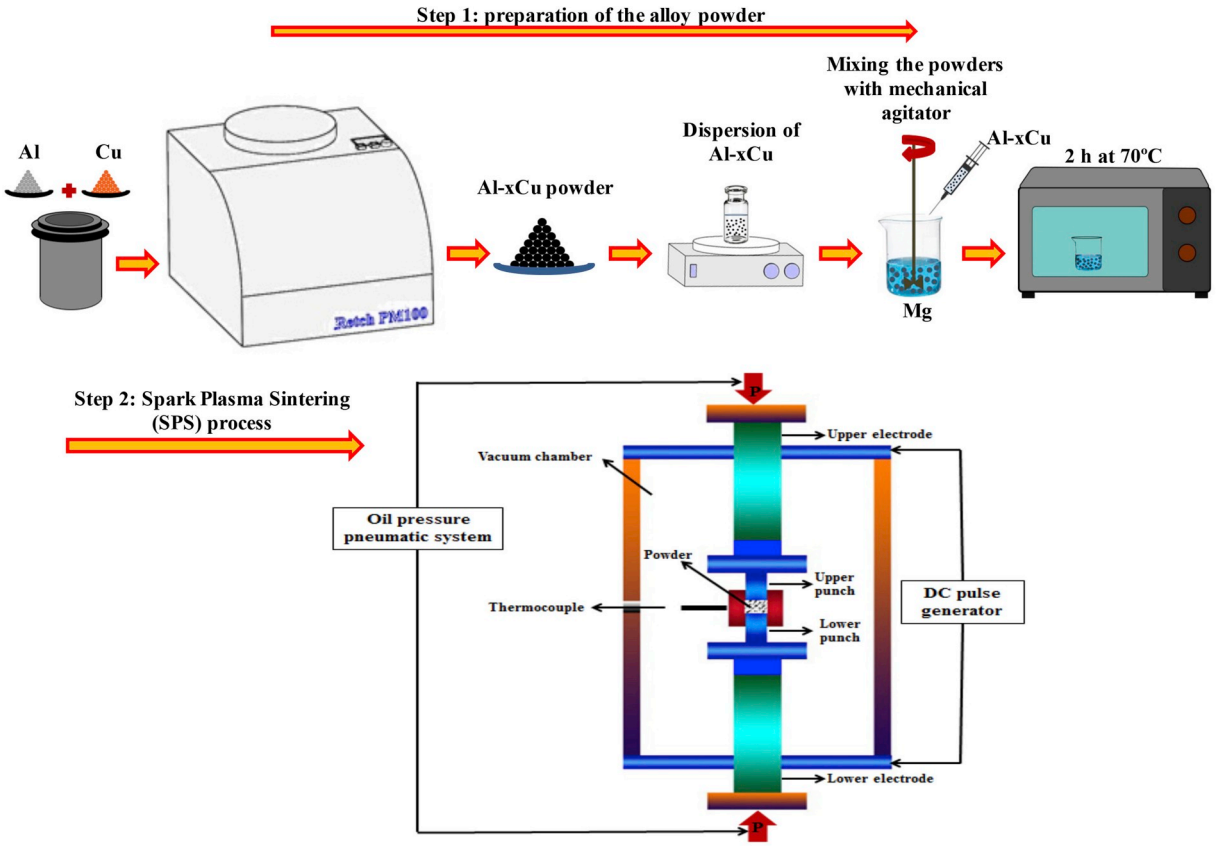

Fig. 1. The schematic of the fabrication of Mg–Al–Cu alloys.

microstructures were investigated using a Digital Keyence VH-Z100 optical microscope.

Uniaxial compression testing was conducted with a HounsField H25KS machine at a parallel orientation compared to the SPS loading direction. In this regard, the samples with the dimension of $3 \times 3 \times 6$ mm (n = 3) were fabricated and mechanical test was performed according to ASTM E9-89a (2000) standard. After plotting the stress-strain curves, the mechanical properties consisting of compressive strength and yield strength were calculated. It needs to mention that the yield strength was measured from the end of the linear region (the final point of the linear region).

2.4. Degradation rate evaluation

The degradation rate of Mg and Mg–1Al–xCu samples was investigated in simulated body fluid (SBF) solution, according to the ASTM-G31-72 [42]. In this regard, the samples with the dimension of $8 \times 6 \times 2$ mm were soaked in SBF solution at 37 °C and pH = 7.4, while the surface area of samples to SBF volume ratio was kept constant. At the specific time points, the corrosion products formed on the surfaces of samples were studied by XRD, SEM and EDS techniques. Moreover, the pH value of the SBF solution, degradation rate, weight loss and the hydrogen release rate were examined during the soaking experiment. Hydrogen release from each sample was estimated using a homemade setup, schematically presented in supplementary Fig. S1. In addition, degradation rate (mm/h) were evaluated, according to ASTM-G31-72, as below(Eq. (1)) [43]:

$$\text{Degradation rate} = \frac{W}{A \times T \times D} \tag{1}$$

where the W is the weight loss (g), A is the sample area exposed to solution (cm^2), T is the exposure time (h) and D is the density (g cm^{-3}). Moreover, the weight loss in each samples was determined by Eq. (2) [44]:

$$Weight\ loss(\%) = \frac{W_1 - W_2}{W_1} \times 100 \tag{2}$$

where W_1 and W_2 are the weight of samples, before and after immersing in SBF.

2.5. Cell culture

The cytotoxicity of Mg–1Al–xCu samples was evaluated on the MG63 osteoblast-like cell (purchased from the National Cell Bank of Iran (NCBI code: C555)). Prior to cell culture, the samples were sterilized in 70 vol% ethanol followed by 2 h exposure to UV light. MG63 cells were cultured in Dulbecco's Modified Eagle Medium (DMEM-low glucose, Bioidea, Iran) supplemented with 10 vol% fetal bovine serum (FBS) (Bioidea, Iran) and 1 vol% streptomycin/penicillin (Bioidea, Iran) at 37 °C with 5% CO_2.

The cytotoxicity assay was assessed via a dilution of Mg–1Al–xCu extracts (0.12 mg/ml) in contact with MG63 cells (ISO/EN 10993.5, 1999). This concentration was determined according to the primary results obtained from various concentrations of Mg–1Al–xCu extracts (0.25, 0.18, 0.12, 0.06, 0.03 mg/ml). Inductively coupled plasma atomic emission spectrometry (PerkinElmer ICP-AES) was employed to measure the concentration of Mg and Cu ions which were dissolved from the alloys. For cell culture experiments, the MG63 cells were seeded on the 96-well plates with density of 6×10^3 cells/well. Consequently, after 24 h incubation at 37 °C, the medium was discard and replaced with diluted extracts of the samples.

The cytotoxicity of samples was considered by 3-(4,5-dimethylthiazolyl-2)-2,5-diphenyl tetrazolium bromide (MTT, Sigma-Aldrich) assay. At the specific culture time (1 and 3 days), the culture medium

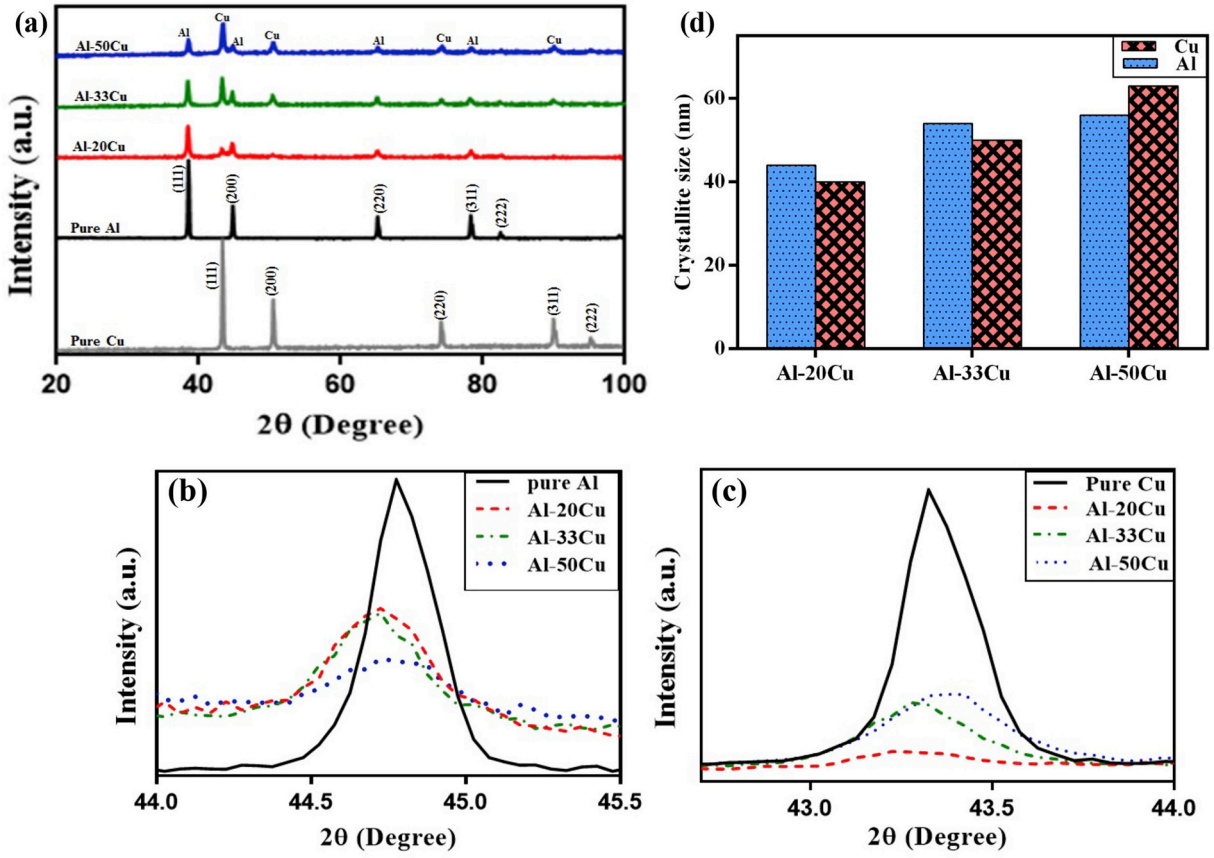

Fig. 2. XRD patterns of a) pure powders (Al and Cu) before milling and Al-xCu (x = 20,33 and 50) powders after 20 h milling, b) (200) crystal plane of Al and c) (111) crystal plane of Cu. d) The crystallite size of Al and Cu in Al-xCu (x = 20, 33 and 50) powders, after 20h milling.

was discarded from the samples and was replaced with MTT solution (0.5 mg/ml MTT reagent in phosphate buffered saline (PBS)). After 4h incubation, the formazan crystals were dissolved in dimethyl sulfoxide (DMSO, Sigma) and the optical density (OD) of the solutions were quantified with a microplate reader (Bio Rad, Model 680 Instruments) against DMSO (blank) at a wavelength of 490 nm. Finally, the relative viability of the cells was calculated based on the equation [45]:

$$\text{Relative cell survival } (\%) = \frac{A_{sample} - A_b}{A_{control} - A_b} \times 100 \quad (3)$$

where A_{sample}, A_b and $A_{control}$ are the absorbance of sample, blank (DMSO) and control (tissue culture plate (TCP)), respectively.

2.6. Antibacterial property

The antibacterial property of the Mg–1Al-xCu alloy extracts was examined by the disc diffusion method using *Staphylococcus aureus* (*S. aureus*) and *Escherichia coli* (*E. coli*) bacteria. The Mg–1Al-xCu alloy extracts with the concentration of 0.25 g/ml were prepared similar to the protocol applied for cytotoxicity test. The bacteria stock solution was made by mixing 5–10 colony bacteria population and incubated at 37 °C for 24 h. The bacterial suspensions were consequently added to Brain heart infusion (BHI) agar plate. After that, some holes were created in

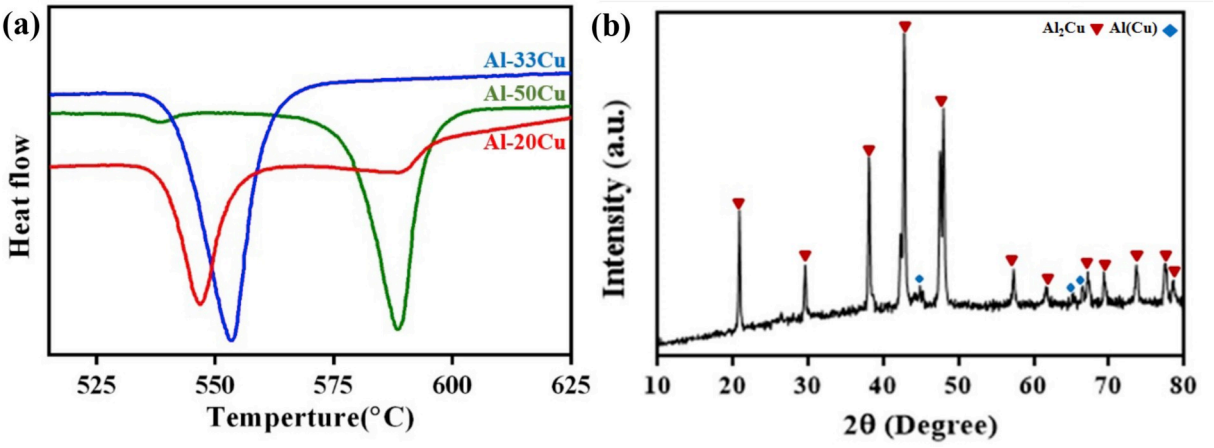

Fig. 3. a) DTA curves of Al-xCu powders (x = 20,33 and 50). b) XRD pattern of Al–50Cu sample.

the center of the plate and then the alloy extracts were inserted in the holes. The samples were kept at 37 °C for 24 h and consequently the diameter of inhibition zone was calculated to investigate the antibacterial property of the Mg–1Al-xCu alloys.

2.7. Statistical analysis

The data was studied via one-way ANOVA analyses and stated as the mean ± standard deviation (SD). Moreover, Tukey's post-hoc test (GraphPad Prism Software (V.6)) was applied to establish a statistical significant difference between groups (p-value <0.05).

3. Results and discussion

3.1. Characterization of Al-xCu powders

Before the fabrication of Mg–Al-xCu alloy via SPS approach, the milled Al-xCu powder was analyzed. The XRD patterns of the milled powders (Fig. 2a) confirmed that 20h-milling process did not result in the formation of new phases. All patterns consisted of Al and Cu characteristic peaks, with various intensities, depending on the chemical compositions of powder. Results showed that the intensity of the Cu characteristic peaks enhanced with increasing Cu content. Furthermore, according to the characteristic peak of Al at $2\theta \approx 44.7°$ ((200) crystal plane)(Fig. 2b), a peak displacement to lower angles was occurred compared to that of pure Al, indicating that the Cu elements with larger atomic radius diffused in Al structure [46]. Moreover, the intensity of the characteristic peak of Cu at $2\theta \approx 43.4°$ ((111) crystal plane) (Fig. 2c) reduced after milling process, showing that Cu element was penetrated in Al lattice. Nemati et al. [47] similarly studied on the Al-4.5 wt% Cu alloy prepared by ball milling method and found that Cu atoms could penetrate in Al lattice structure. According to Fig. 2b and c, the broadening of peaks was also happened in Al and Cu characteristic peaks after milling process, which could be due to the grain refining. It might be due to the reduction in the crystallite size and enhanced lattice strain because of sever deformation [48]. To study the effect of Cu content on the crystallite size of the powders, the Williamson–Hall method was employed. The changes in the crystallite size of Al and Cu in various Al–Cu compositions after 20h milling process are presented in Fig. 2d. Results showed that the crystallite size of both Al and Cu powders enhanced with increasing Cu content. It might be due to the ductile nature of Cu element showing a good cushioning effect during the milling of Al-xCu powders [48]. Consequently, addition of Cu in Al prevented from reduction in the crystallite size of powders, during the milling process.

In order to anticipate the chemical composition of Al–Cu powders during SPS process, DTA analysis was performed. According to the DTA curves (Fig. 3a), during the heating process, one or two endothermic reactions (the negative peaks) were occurred, depending on the powder composition. It needs to mention that, according to Al–Cu phase diagram, Al–20Cu, Al–33Cu and Al–50Cu are hypoeutectic alloy, eutectic alloy and hypereutectic alloy, respectively [49]. The DTA curve of hypoeutectic alloy (Al–20Cu) (Fig. 3a) consisted of two endothermic peaks at 546 °C and 580 °C, related to the proeutectic Al(Cu) and Al–Al_2Cu eutectics reaction, respectively. Moreover, DTA curve of Al–33Cu (eutectic alloy) consisted of only one peak at 550 °C, corresponded to the eutectic reaction (equilibrium temperature of Al–Al_2Cu eutectics is 548 °C). Finally, DTA curve of the Al–50Cu (hypereutectic alloy) consisted of two peaks at 541 °C and 590 °C which might be related to peritectoid reaction and proeutectic Al_2Cu phase formation, respectively [49]. In order to confirm these results, the Al–50Cu bulk (hypereutectic alloy) was separately fabricated by SPS technique at 600 °C and 40 MPa pressure for 10 min. XRD pattern of Al–50Cu alloy (Fig. 3b) consisted of the characteristic peaks of Al_2Cu intermetallic phase and Al(Cu) component, confirming DTA analysis curves.

Fig. 4a–c shows SEM images and EDS analysis of Al–Cu powders containing various amounts of Cu content, after 20 h milling. In order to evaluated the changes in the morphology of Al–Cu powders during milling process, the SEM images of the primarily Al and Cu powders were similarly investigated (Supplementary Fig. S2 a, b). Al and Cu powders consisted of irregular-shape and branch-like particles, respectively. After 20h milling, the morphology of initially powders was completely changed to plate-like. The similar morphology was reported for Al-4.5 wt% Cu alloy after 40 h mechanical milling, in a previous research [47]. Moreover, increasing in the particle size of powders could be detected, indicating that deformation and cold welding occurred during the milling process [46]. Resulted showed that, the particle size of Al–20Cu, Al–33Cu and Al–50Cu powders was estimated about 92 ± 21 μm, 96 ± 24 μm and 117 ± 20 μm, respectively. It could be found that, the particle size of powders enhanced with increasing Cu content, which could be due to the ductile nature of Cu leading to less hard-working during milling process. Moreover, the EDS analyses of Al-xCu powders indicated that any impurity was not incorporated in the milled powders.

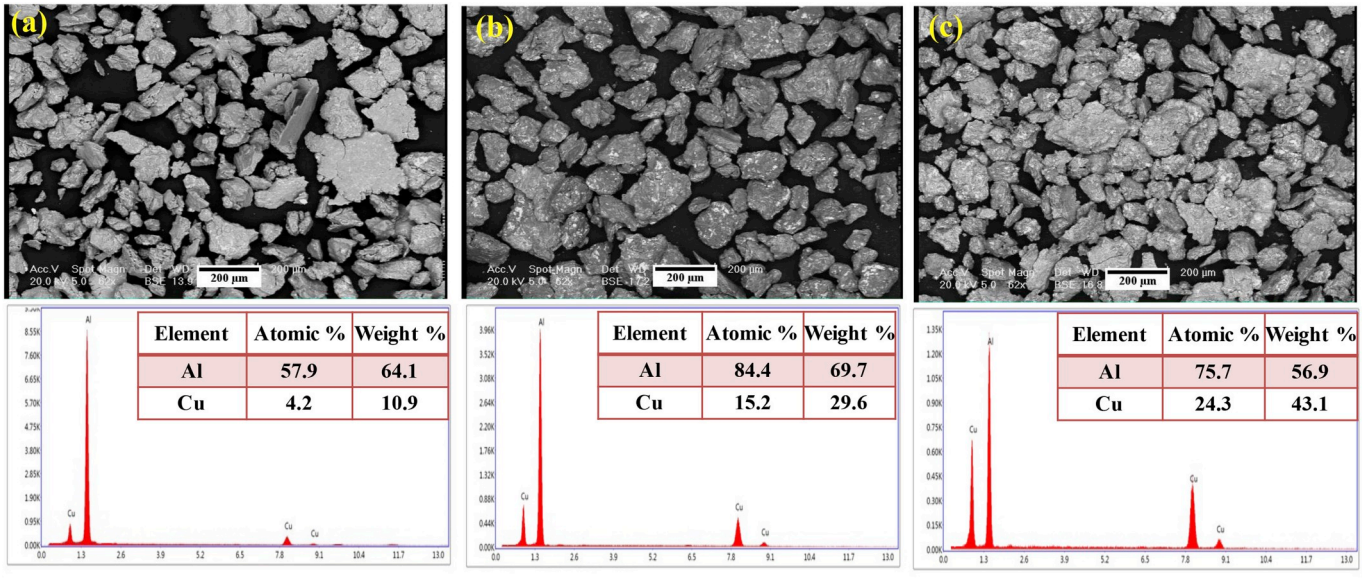

Fig. 4. SEM images and EDS analysis of Al-xCu powders consisting of various amounts of Cu: a) x = 20, b) x = 33 and c) x = 50.

3.2. Characterization of Mg–1Al-xCu alloy

After evaluation of Al-xCu powders, ternary alloy of Mg–1Al-xCu was fabricated via SPS process. SEM images and EDS-mapping analysis of Mg–1Al-xCu alloy are presented in Fig. 5. Moreover, High magnification SEM images and EDS analysis of Mg–1Al-xCu alloys (x = 0, 0.25 and 1 wt %) in two difference area (points 1 and 2 in the SEM images) are provided in Fig. 6. According to the SEM images (Fig. 5a), the secondary phases distributed in the matrix of all samples. However, the chemical composition of the secondary phases was different, depending on the samples type. For instance, according to the formation of eutectic phase of Mg and Al elements at 450 °C [50], the white precipitates in Mg–1Al were the eutectic Mg(Al) phase developed during the SPS process. In another word, SEM and EDS-mapping of Mg–1Al-xCu alloys also revealed the formation of white precipitations. Based on DTA curves (Fig. 3a), the Al_2Cu and eutectic composition (α-Al_2Cu) was synthesize in Mg–1Al-xCu alloying, during SPS process. Consequently, the white precipitations in Mg–1Al-0.25Cu and Mg–1Al–1Cu alloys were Al_2Cu phase which were formed at 580 °C and 590 °C, respectively, during the SPS process (Fig. 3). XRD patterns of Mg–1Al-0.25Cu and Mg–1Al–1Cu alloys also confirmed the formation of Al_2Cu phase during SPS process (Supplementary Fig. S3). Moreover, based on EDS-mapping analysis of Mg–1Al-xCu (x = 0.25 and 1 wt%) (Fig. 5b), this secondary phase was uniformly distributed in the matrix. High magnification SEM images and EDS analysis of Mg–1Al-0.25Cu and Mg–1Al–1Cu alloys (Fig. 6) also revealed that Cu and Al elements distributed in white precipitates and these precipitates scattered in Mg matrix alloy. According to EDS analysis, the weight ratio of Mg/Al, Mg/Cu and Cu/Al in various points of samples were determined (Fig. 6b). Results revealed that while the point "1" in both Mg–1Al-0.25Cu and Mg–1Al–1Cu alloys was Mg-rich, few amounts of Al and Cu penetrated in Mg matrix. The weight ratio of Cu/Al in the first area of Mg–1Al-0.25Cu and Mg–1Al–1Cu alloy was 0.7 and 1.25, respectively. Therefore, with increasing Cu content in Mg–1Al-xCu alloy, the amount of Cu penetration in Mg matrix alloy increased. Moreover, the point "2" in Mg–1Al-xCu (x = 0.25 and 1 wt%) alloy was rich of Al and Cu. In these points, the weight ratio of Cu to Al elements increased from 1.7 in Mg–1Al-0.25Cu alloy to 3.9 in Mg–1Al–1Cu alloy. In another word, SEM images of Mg–1Al-0.5Cu alloy revealed the presence of different precipitates with coarser size compared to those of Mg–1Al-0.25Cu and Mg–1Al–1Cu alloys. These precipitates revealed a layered structure which might be related to the eutectic composition of Al and Cu (α-Al_2Cu), according to the DTA curve (Fig. 3a). In addition, EDS mapping analysis of Mg–1Al-0.5Cu alloy showed the presence of Cu-rich layer in the core and Al-rich layer in the

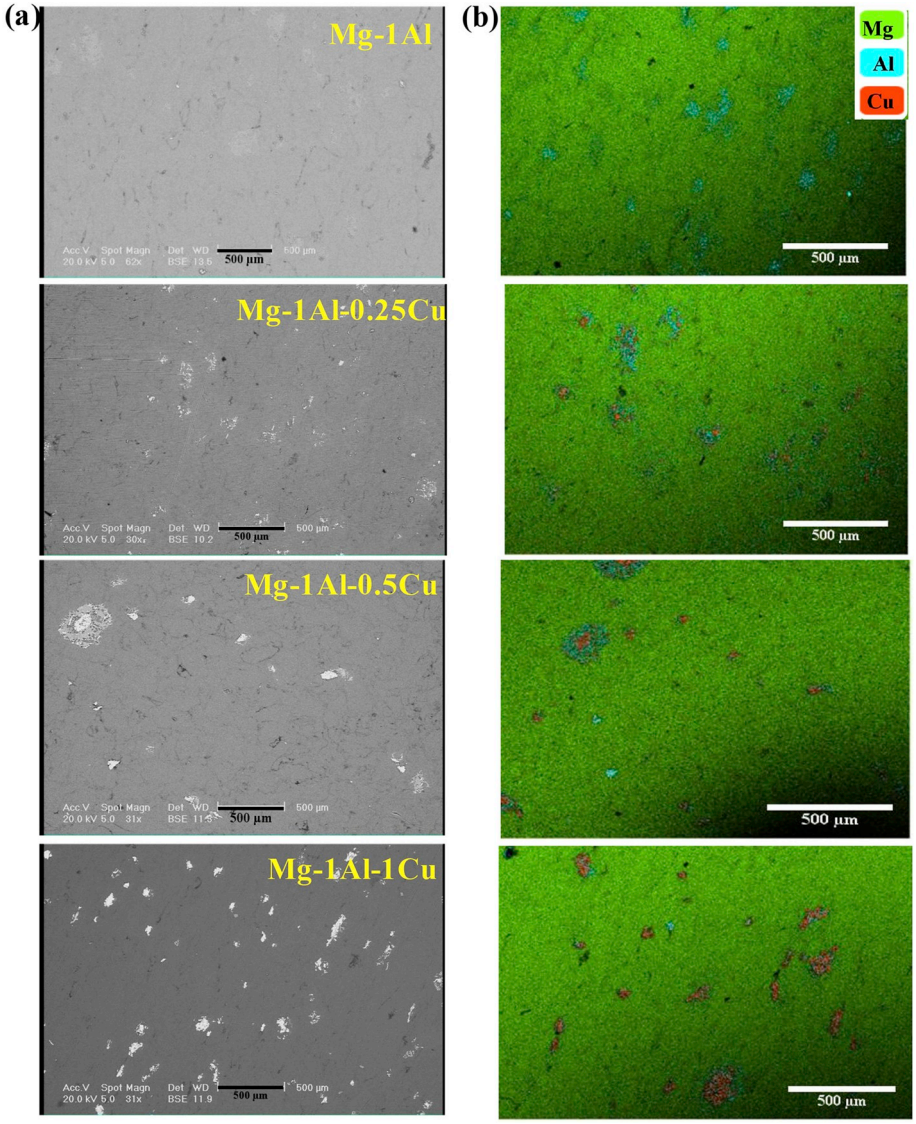

Fig. 5. a) SEM images and b) EDS mapping analysis of Mg–1Al-xCu (x = 0, 0.25, 0.5 and 1) alloy.

(a)

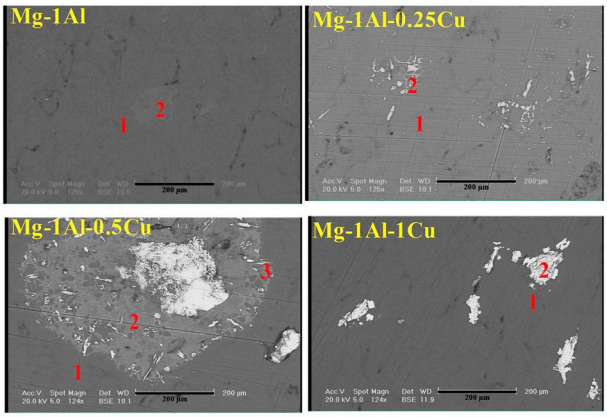

(b)

Material	Weight ratio	Area 1	Area 2	Area 3
Mg-1Al	Mg/Al	12.98	1.14	-
Mg-1Al-0.25Cu	Mg/Al	6.7	1.6	-
	Mg/Cu	10	0.9	-
	Cu/Al	0.7	1.7	-
Mg-1Al-0.5Cu	Mg/Al	10.25	0.36	1.3
	Mg/Cu	8.2	0.86	0.56
	Cu/Al	1.25	0.41	2.4
Mg-1Al-1Cu	Mg/Al	10.98	1.4	-
	Mg/Cu	6.38	0.4	-
	Cu/Al	1.72	3.9	-

Fig. 6. a) High magnification SEM images and b) EDS analysis of Mg based alloys.

shell of these precipitates. EDS analysis also similarly showed that these precipitations consisted of two distinct Al and Cu rich layers. Moreover, the major of the first area consisted of Mg elements, which few amount of Al and Cu elements penetrated in it.

The relative dense structure of the Mg–1Al-xCu (x = 0.25, 0.5 and 1 wt%) alloys in addition to the formation of the secondary phase could have significant role on the mechanical properties of the samples. Fig. 7a shows the stress-strain curves of pure Mg and Mg–1Al-xCu alloys fabricated by SPS process. Results showed that the compressive strength and yield strength enhanced with increasing Al and Cu elements. The compressive and yield strength of samples were extracted from stress-strain curves (n = 3) and are presented in Fig. 7b and c. It could be found that both compressive and yield strength enhanced after incorporation of 1 wt% Al. It could be due to the formation of Mg(Al) solid solution and secondary phases during SPS process. The strengthening mechanism of Mg–1Al alloy resulted from the interaction between the dislocations and the solute atoms (dislocation strengthening mechanism) [51]. The alloying elements make plastic deformation more difficult by impeding dislocation motion or decreasing the energy barrier for cross-slip of dislocations [52]. In this mechanism, the movement of dislocations in the matrix alloy could be hindered by Mg(Al) solid solution. Moreover, based on Fig. 7, the compressive and yield strength

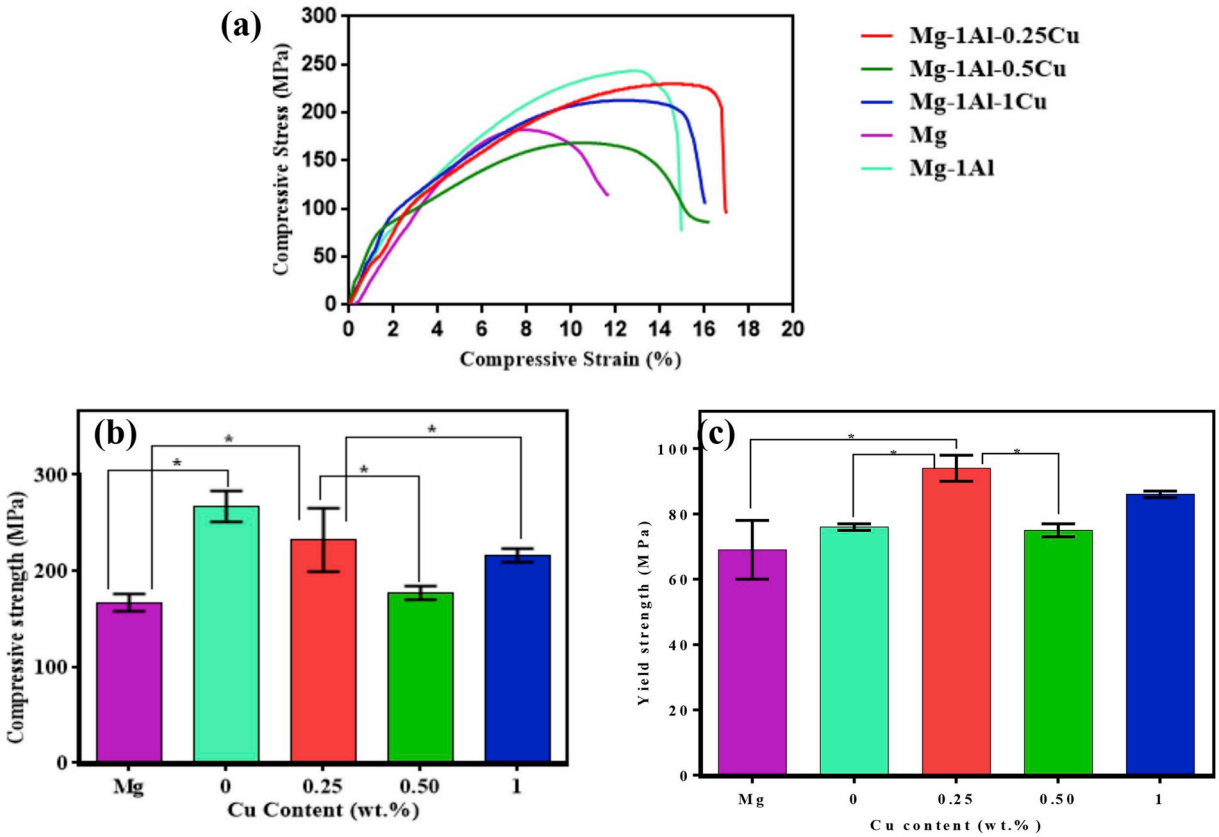

Fig. 7. Mechanical properties of pure Mg and Mg–1Al-xCu (x = 0, 0.25, 0.5 and 1) alloys: a) compressive stress-strain curves as well as b) compressive strength and c) yield strength of alloys, as a function of Cu content (*P < 0.05).

enhanced in Mg–1Al-0.25Cu (232 ± 3 MPa and 94 ± 4 MPa, respectively) compared to pure Mg (167 ± 9 MPa and 69 ± 9 MPa, respectively). It might be attributed to the uniform distribution of Al_2Cu precipitates. According to our previous results, Al_2Cu is an intermetallic phase with higher strength (about 660 MPa), 0.2% yield strength (440 MPa) and Young's modulus (88 GPa) [53], than those of alloy matrix. In a similar research, Homayun et al. [60] showed the role of intermetallic particles in mechanical properties of Mg based alloy. They investigated the mechanical properties of Mg–4Zn-xAl-0.2Ca (x = 0–3 wt%) alloy and showed that incorporation of Al and Zn elements could promote the mechanical characteristics of Mg via solid-solution strengthening and microstructure refinement mechanisms. In this research, the $Ca_2Mg_6Zn_3$ secondary phase formed in grains boundary leading to enhanced strength from 157 MPa (in Mg–4Zn-0.2Ca) alloy to 198 MPa (in Mg–4Zn–3Al-0.2Ca alloy). In addition, the volume fraction and size of precipitates also affected the mechanical properties of the alloys, as similarly reported in previous research [54]. According to Fig. 7, the Mg–1Al-0.25Cu with a more uniform distribution of Al_2Cu particles in the grain boundary revealed the greater compressive and yield strength than those of Mg–1Al-0.5Cu alloy (177 ± 7 MPa and 75 ± 2 MPa, respectively). Similarly, Hassn et al. [55] found that the Mg–Cu alloy consisting of 17.95 wt% Cu improved the mechanical properties compared to pure Mg, due to well distribution of Mg_2Cu in the matrix. In other research, Trojanova et al. [56] indicated that addition of Al to Mg–4Li alloy resulted in the formation of Al_2Li and $Mg_{17}Al_{12}$ secondary phases leading to improved mechanic properties of alloy according to the precipitation hardening mechanism.

The degradation behavior of pure Mg and Mg–1Al-xCu (x = 0, 0.25, 0.5 and 1 wt%) alloy was studied by immersion test. The samples (n = 3) were soaked in SBF solution at 37 °C for 10 h and the volume of released hydrogen gas, pH value of SBF solution and changes of sample weight were recorded (Fig. 8). Generally, when Mg based materials are immersed in aqueous solutions, the following reactions occurred [57]:

$$Mg \rightarrow Mg^{2+} + 2e \quad \text{(Reaction 1)}$$

$$2H_2O + 2e \rightarrow H_2 + OH^- \quad \text{(Reaction 2)}$$

$$Mg^{2+} + OH^- \rightarrow Mg(OH)_2 \quad \text{(Reaction 3)}$$

$$Mg^{2+} + 2Cl^- \rightarrow MgCl_2 \quad \text{(Reaction 4)}$$

$$Mg(OH)_2 + 2Cl^- \rightarrow MgCl_2 \quad \text{(Reaction 5)}$$

At first, Mg dissolved in SBF solution, leading to formation of Mg^{2+} ions (reaction 1). As the same time, cathodic reaction (reaction 2) was occurred and galvanic corrosion started. Therefore, according to these reactions, the volume of released hydrogen directly related to the degradation rate of Mg based materials. Consequently, these results could provide a trusty method to investigate the corrosion properties of Mg [58]. According to the photograph images of various samples after 10h immersion (Fig. 8a), it could be found that there was a significant difference between the surface morphology of samples, depending on their chemical composition. With increasing Cu and Al elements, the corrosion products deposited on the surface of samples were noticeably enhanced. In addition, according to Fig. 8b, the average volume of released hydrogen per surface significantly reduced from 1.61 ml/cm^2 (in pure Mg) to 0.41 ml/cm^2 (for Mg–1Al alloy). In another word, the weight loss and degradation rate of Mg–1Al alloy (Fig. 8c) significantly

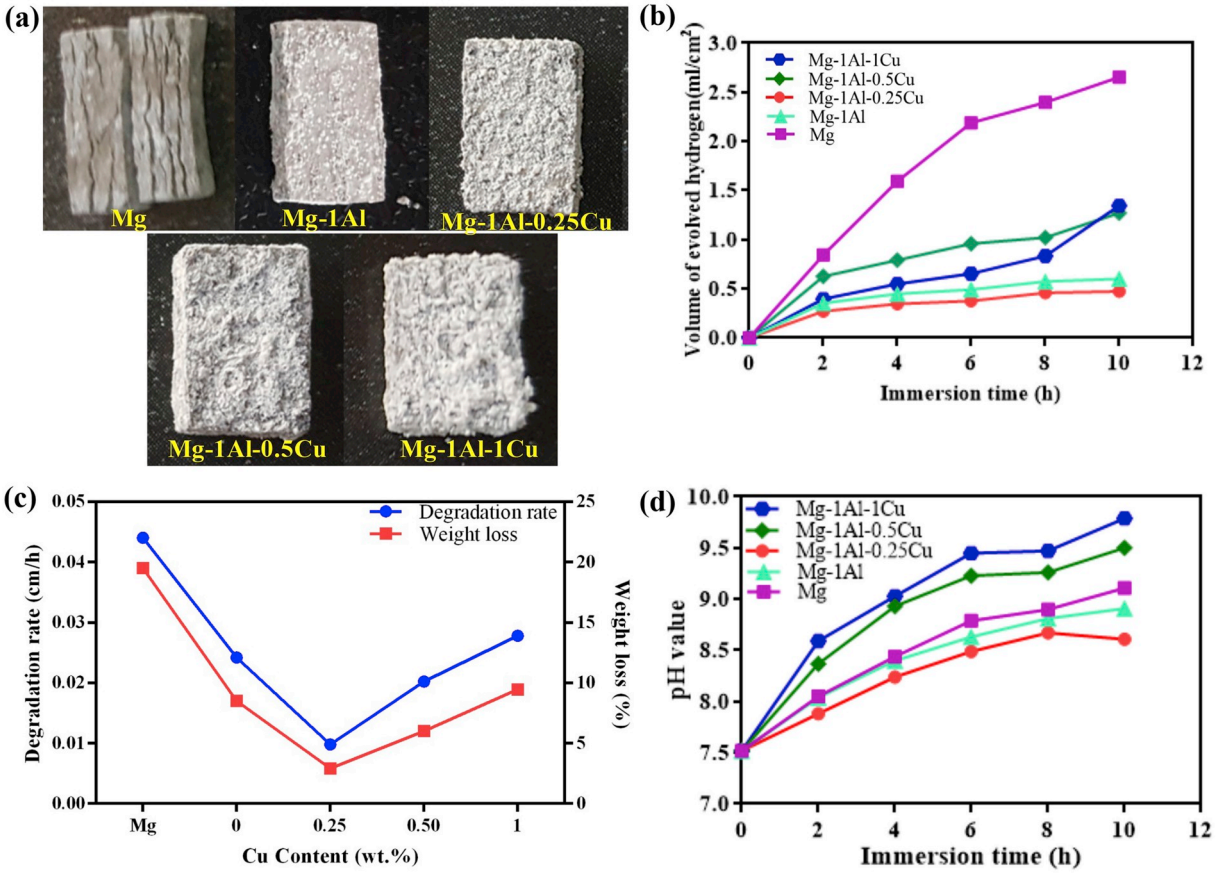

Fig. 8. Degradation evolution of Mg and Mg–1Al-xCu alloy (x = 0, 0.25, 0.5 and 1 wt%) in SBF solution: a) Photograph images of pure Mg and Mg–1Al-xCu alloy after 10h soaking in SBF solution. b) The volume of released hydrogen, c) weight loss and average weight loss of samples and d) pH value of SBF solution during the soaking of samples.

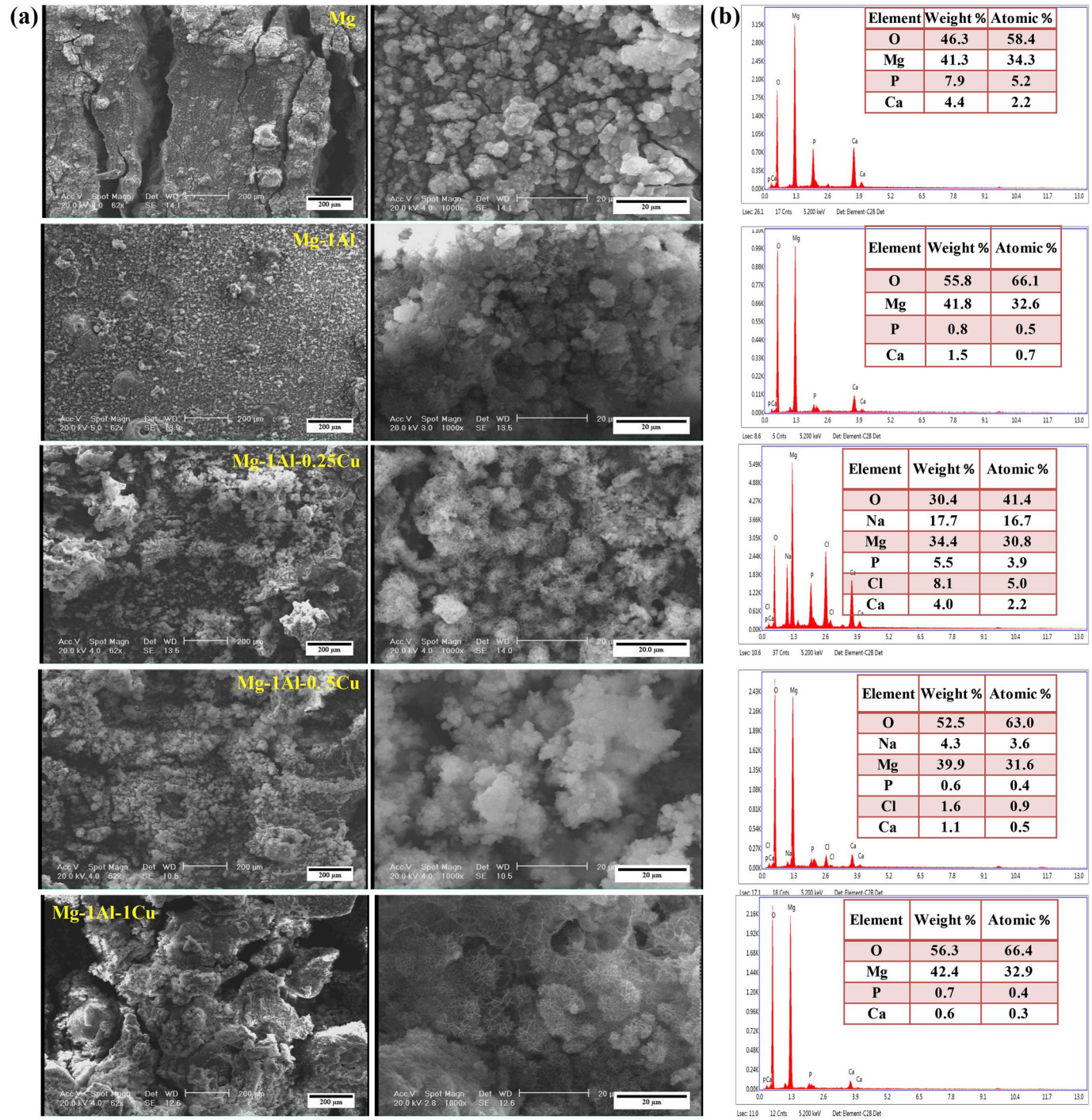

Fig. 9. Degradation evolution of Mg and Mg–1Al-xCu alloys (x = 0, 0.25, 0.5 and 1 wt%) in SBF solution: a) SEM images and b) EDS spectra of pure Mg and Mg–1Al-xCu after 10h soaking in SBF solution.

reduced from 22% to 0.039 cm/h to 12.1% and 0.017 cm/h, respectively. Finally, the pH value of SBF solution was also significantly improved during the immersion of Mg sample, compared to Mg–Al alloy confirming the higher release of OH^- ions and consequently greater degradation rate [59]. Chun et al. [60] also investigated the degradation behavior of AZ31, via immersing in Hanks' solution at 37 °C. They found that the volume of released H_2 decreased from 20 ml/cm^2 to 2 ml/cm^2, when Mg was replaced with AZ31 alloy. As a consequence, the presence of Al reduced the corrosion rate of Mg. It could be due to the similarity between the potential corrosion of alloy matrix and Mg(Al) phase which prevented from the galvanic corrosion of Mg–1Al. Furthermore, the significant differences in the degradation performance of pure Mg and the Mg–1Al-xCu alloys could be detected. Noticeably, the average volume of released H_2 decreased to 0.32 ml/cm^2 in Mg–1Al-0.25Cu alloy compared to pure Mg (1.61 ml/cm^2). In addition, the degradation rate and weight loss of Mg–1Al-0.25Cu alloy (Fig. 8c) significantly reduced to 0.0058 cm/h and 4.9%, respectively. Moreover, the pH value of SBF solution during immersing of Mg–1Al-0.25Cu alloy did not significantly change, compared to other samples confirming the reduced degradation rate. Improved corrosion resistance of Mg–1Al-0.25Cu alloy could be due to the formation of fine Al_2Cu precipitates which were uniformly distributed in the grain boundary. However, our results demonstrated

that the corrosion resistance decreased with more increasing Cu content from 0.25 wt% to 1 wt%. For instance, the degradation rate and weight loss of Mg–1Al–1Cu was 0.019 cm/h and 13.9%, respectively, which were greater than those of Mg–1Al-0.25Cu alloy. It could be due to the formation of Al_2Cu and α-Al_2Cu precipitates in the Mg–1Al-xCu alloy acting as cathode points to stimulate the degradation rate of alloy. The role of size and distribution of precipitates on the degradation properties of Mg based alloy was similarly reported in previous researches [61]. Liu et al. [30] investigated the effect of Cu content on the degradation of Mg-xCu alloy (x = 0.03, 0.19 and 0.57 wt%) and found that the volume of released H_2 and degradation rate of Mg–Cu alloy enhanced with increasing Cu content due to the galvanic corrosion occurred in the presence of coarse precipitates in the Mg matrix.

SEM images of pure Mg and Mg–1Al-xCa (x = 0, 0.25, 0.5 and 1 wt%) alloys after 1h soaking in SBF solution are provided in Fig. 9a. The formation of deep cracks on the surface of pure Mg confirmed that the integrity of the sample was destroyed during the immersing in SBF solution. In contrary, the surface of Mg–1Al-xCu alloys was covered with the corrosion product layers and the surface crack could not be detected on the surface. According to EDS analysis, the corrosion product consisted of magnesium, oxygen, phosphorus and calcium ions indicating the formation of magnesium hydroxide [$Mg(OH)_2$] and Ca–P granules on the samples. According to XRD pattern of Mg–1Al-xCu alloy after immersion test (Fig. 10), these precipitates consisted of hydroxyapatite (HA) and $Mg(OH)_2$ phases formed during the soaking in SBF solution. In addition to these ions, Cl^- ions were deposited on the sample surfaces. Based on reactions 3–5, the $Mg(OH)_2$ could change to $MgCl_2$, due to the presence of Cl^- ions in SBF solution. Dissolution of $Mg(OH)_2$ caused to release OH^- ions as indirect corrosion products [11]. In addition, the PO_4^{3-}, HPO_4^{2-}, $H_2PO_4^-$ and Ca^{2+} ions presented in SBF solution reacted with OH^- ions leading to formation of Ca–P nodules on the surface of samples, as similarly reported in previous researches [57]. Moreover, the morphology of corrosion products was cauliflower and needle shapes, which were similar to the apatite deposited in the matrix of collagen in human bones [62]. These unique structure could provide larger surface to form more HA deposition on the surface of Mg–1Al-xCu alloys [63].

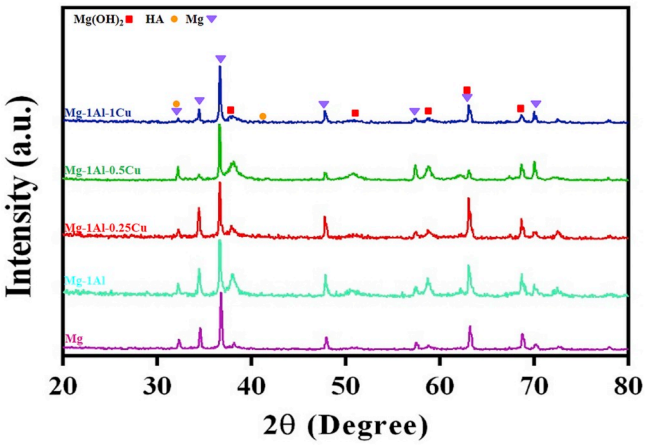

Fig. 10. XRD pattern of Mg–1Al-xCu alloy (x = 0, 0.25, 0.5 and 1 wt%) after 10h soaking in SBF solution.

3.3. Biological properties of Mg–1Al-xCu alloys

MTT assay was performed to assess the metabolic activity of MG63 cells cultured on the extracts of pure Mg and Mg–1Al-xCu (x = 0, 0.25, 0.5 and 1 wt%) alloys. Fig. 11a shows the cell viability after 1 and 3 days of culture on the extracts of samples. The Cu and Mg ion concentration in the extracts of alloys are presented in Fig. 11b. It could be found that the concentration of Mg and Cu ions enhanced with increasing Cu content in the Mg–1Al-xCu alloys. According to Fig. 11a, the viability of MG63 cells slightly enhanced with increasing culture time on the various samples, showing that all samples were not toxic. Between them, Mg–1Al-0.25Cu alloy significantly improved MG63 cell viability from day 1 to day 3 ($P < 0.05$). In another word, incorporation of Cu in Mg–1Al alloy significantly improved cell proliferation, depending on the Cu concentration. Noticeably, after 3 days of culture, the viability of cells cultured on the Mg–1Al-0.25Cu (161.3 ± 11.8 % control) significantly enhanced compared to that of on the pure Mg (129.2 ± 9.6 %control) and Mg–Al (108.5 ± 2.3 %control) ($P < 0.05$). However, increasing amounts of Cu in Mg–1Al-xCu reduced the proliferation of MG63 cells to 68.4 ± 5.2 %control (in Mg–1Al–1Cu) ($P < 0.05$) which might be due to the greater concentration of Cu and Mg ions in the culture medium (Fig. 11b). It could be concluded that while the lower Cu concentration in the Mg–1Al-0.25Cu improved the cell proliferation, incorporation of more Cu in Mg–1Al-xCu alloy resulted in reduced cell growth. Cu ions are powerful antioxidant which could destroy the free radicals to improve biological properties [64]. However, at high concentrations of Cu ions, the cell membrane was damaged leading to cell death, as similarly reported in previous researches [65]. In a similar research, Liu et al. [30] suggested that the cytotoxicity of Mg-xCu alloys (x = 0.03, 0.19 and 0.57 wt%) was related to Cu concentration and the biocompatibility of the alloys reduced with increasing Cu concentration.

The antimicrobial activity of the pure Mg and Mg–1Al-xCu alloys was also considered via the disc diffusion test against to *E. coli* and *S. aureus* bacteria (Fig. 12). It could be found that pure Mg executed antibacterial

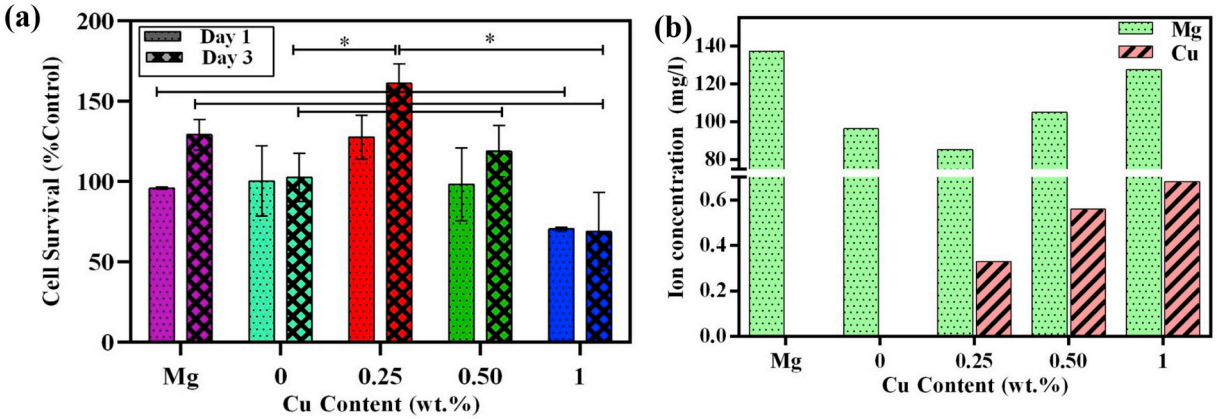

Fig. 11. Biological responses of Mg and Mg–1Al-xCu alloy (x = 0, 0.25, 0.5 and 1 wt%): a) Viability of MG63 cells on pure Mg and Mg–1Al-xCu alloys consisting of various amounts of Cu content using MTT assays, after 1 and 3 days of culture (*$P < 0.05$). b) Mg and Cu ion concentrations released into extracts.

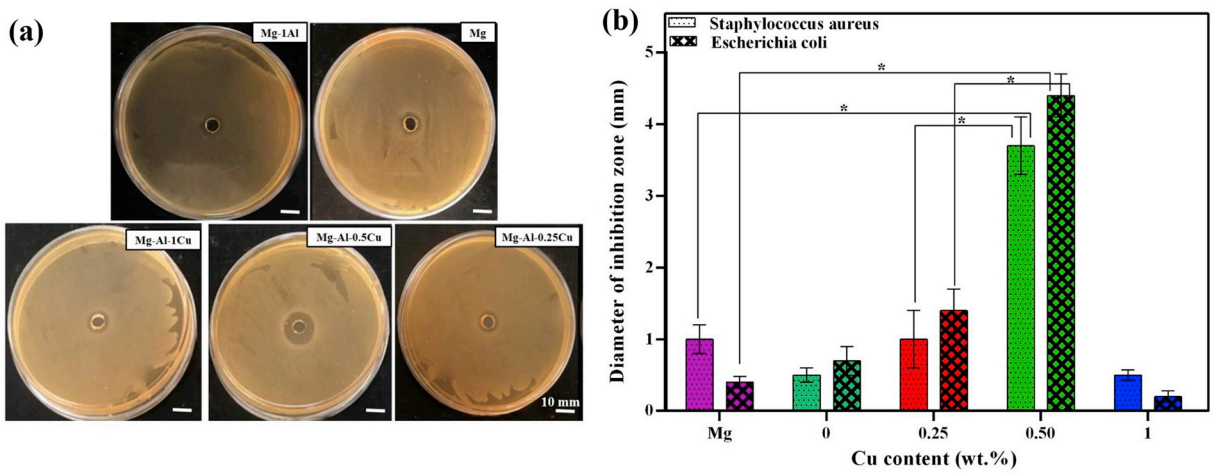

Fig. 12. Antibacterial activity of Mg and Mg–1Al-xCu alloy (x = 0, 0.25, 0.5 and 1 wt%): a) Inhibition zones around Mg–1Al-xCu alloys consisting of various amount of Cu, against *E. coli* bacteria. b) Dimension of inhibition zone of Mg–1Al-xCu alloys consisting of various amounts of Cu against *E. coli* and *S. aureus* bacteria(*P < 0.05).

activity against the bacteria which might be related to the increased pH of extracts during the degradation of Mg. Previous researches confirmed that bacteria could be alive usually in the pH range between 6 and 8, in which bacteria could keep a cytoplasmic pH [66]. In a research, Ren et al. [67] investigated the antibacterial activity of pure Mg and Mg alloy (AZ31) against *E. coli* and *S. aureus* bacteria. In this research, the pH values of both bacterial suspensions with Mg and AZ31 alloy increased from 7.4 to 10 and 9.5 after 24 h, respectively. The results indicated the antibacterial function of Mg and AZ31 as the *E. coli* and *S. aureus* bacteria would not survive at high pH value (upper than 8). However, as time lapse, the pH value stabilized in the physiological environment. Consequently, long-term infection may not be avoided.

Our results also showed that, Mg–1Al-0.5Cu alloy revealed that greatest antibacterial activity against both Gram-negative (*E. coli*) and Gram-positive (*S. aureus*) bacteria (Fig. 12a). According to Fig. 12b, the dimension of inhibition zone increased from 0.4 ± 0.1 (mm) and 1.0 ± 0.2 (mm) in pure Mg to 4.3 ± 0.3 mm and 3.7 ± 0.4 mm in Mg–1Al-0.5Cu alloy, against *E. coli* and *S. aureus* bacteria, respectively. It might be due to the highest concentration of Cu ions in the extract. The antibacterial mechanism of Mg–1Al-xCu alloys could be occurred via two different strategies. At first, the increasing of pH value due to degradation of Mg based alloys in physiological environment which led to improved antimicrobial properties of Mg–1Al-xCu alloys, as similarly reported above. In another word, the antimicrobial activity could be related to Cu release in degradation extract of Mg–1Al-xCu alloys. The Cu ions could attach to the bacteria cell wall and tear it, leading to protein denaturation and cell death [68]. Although the release of Cu ions could promote the antimicrobial properties of alloys, the antibacterial activity of Mg–1Al-xCu alloys reduced with increasing the amount of Cu content upon 1 wt% (Fig. 12a). It might be due to the changes of pH value of suspension with increasing Cu content. The pH value of suspensions was nearly fixed and the excess amount of copper ion release in Mg–Al–1Cu alloy did not effect the antibacterial properties. Li et al. [27] investigated the effect of Cu ions on the antibacterial ability of pure Mg and found that the addition of 0.25 wt% could prevent from biofilm formation on the Mg based implants.

It could be concluded that between various samples, Mg–1Al-xCu alloy consisting of 0.25–0.5 wt% Cu could provide significant biocompatibility and antibacterial properties making it appropriate for bone degradable implants.

4. Conclusion

In this study, Mg–1Al–Cu alloys were successfully fabricated using spark plasma sintering method and their physical, mechanical, degradation, biological and antibacterial properties were investigated. The following conclusions could be drawn:

1. Incorporation of 0.25 wt% Cu in Mg–1Al alloy resulted in greater compression and yield strength than pure Mg owing to the formation and homogenous distribution of Al_2Cu secondary phase.
2. Incorporation of 0.25 wt% Cu in Mg–1Al alloy resulted in significantly reduced degradation rate than pure Mg after immersion in SBF solution.
3. Mg–1Al-0.25Cu alloy significantly enhance the proliferation of MG63 cells compared to pure Mg and Mg–1Al.
4. Release of bioactive Mg and Cu could synergistically produce long lasting antibacterial effects.

Acknowledgements

The author should have thanked from Iran National Foundation (INSF, Grant no. 94014204) for financial support.

Appendix A. Supplementary data

Supplementary data to this article can be found online at https://doi.org/10.1016/j.matchemphys.2019.121838.

References

[1] S. Bose, S. Tarafder, Acta Biomater. 8 (2012) 1401–1421.
[2] M. Doblaré, J. Garcıa, M. Gómez, Eng. Fract. Mech. 71 (2004) 1809–1840.
[3] S.B. Goodman, Z. Yao, M. Keeney, F. Yang, Biomaterials 34 (2013) 3174–3183.
[4] H. Li, X. Xie, K. Zhao, Y. Wang, Y. Zheng, W. Wang, L. Qin, Acta Biomater. 9 (2013) 8561–8573.
[5] G. Manivasagam, S. Suwas, Mater. Sci. Technol. 30 (2014) 515–520.
[6] M. Salahshoor, Y. Guo, Materials 5 (2012) 135–155.
[7] K. Chen, J. Dai, X. Zhang, Corros. Rev. 33 (2015) 101–117.
[8] Y. Chen, Z. Xu, C. Smith, J. Sankar, Acta Biomater. 10 (2014) 4561–4573.
[9] H.S. Brar, J. Wong, M.V. Manuel, J. Mech. Behav. Biomed. Mater. 7 (2012) 87–95.
[10] X.-b. Zhang, Z.-z. WANG, Y.-j. XUE, W. Qiang, Trans. Nonferrous Metals Soc. China 24 (2014) 3797–3803.
[11] Y. Xin, T. Hu, P. Chu, Acta Biomater. 7 (2011) 1452–1459.
[12] X.-N. Gu, Y.-F. Zheng, Front. Mater. Sci. China 4 (2010) 111–115.
[13] L. Choudhary, R.S. Raman, Acta Biomater. 8 (2012) 916–923.
[14] M. Razavi, M. Fathi, O. Savabi, B.H. Beni, S.M. Razavi, D. Vashaee, L. Tayebi, Appl. Surf. Sci. 288 (2014) 130–137.
[15] M. Rashad, F. Pan, A. Tang, M. Asif, S. Hussain, J. Gou, J. Mao, J. Ind. Eng. Chem. 23 (2015) 243–250.
[16] Z. Li, M. Kawashita, J. Artif. Organs 14 (2011) 163.
[17] O. Charyeva, J. Neilands, G. Svensäter, A. Wennerberg, Open J. Med. Microbiol. 5 (2015) 1.

[18] C.R. Arciola, D. Campoccia, P. Speziale, L. Montanaro, J.W. Costerton, Biomaterials 33 (2012) 5967–5982.
[19] L. Zhang, J. Yan, Z. Yin, C. Tang, Y. Guo, D. Li, B. Wei, Y. Xu, Q. Gu, L. Wang, Int. J. Nanomed. 9 (2014) 3027.
[20] I. Pountos, T. Georgouli, H. Bird, G. Kontakis, P.V. Giannoudis, Expert Opin. Drug Saf. 10 (2011) 935–945.
[21] S. Tavakoli, S. Nemati, M. Kharaziha, S. Akbari-Alavijeh, Colloid Interface Sci. Commun. 28 (2019) 20–28.
[22] E. Tabesh, H. Salimijazi, M. Kharaziha, M. Mahmoudi, M. Hejazi, Surf. Coating. Technol. 364 (2019) 239–247.
[23] K. Jamuna-Thevi, S. Bakar, S. Ibrahim, N. Shahab, M. Toff, Vacuum 86 (2011) 235–241.
[24] H. Chai, L. Guo, X. Wang, Y. Fu, J. Guan, L. Tan, L. Ren, K. Yang, J. Mater. Sci. Mater. Med. 22 (2011) 2525–2535.
[25] D. Tie, F. Feyerabend, N. Hort, D. Hoeche, K. Kainer, R. Willumeit, W. Mueller, Mater. Corros. 65 (2014) 569–576.
[26] H. Qin, Y. Zhao, Z. An, M. Cheng, Q. Wang, T. Cheng, Q. Wang, J. Wang, Y. Jiang, X. Zhang, Biomaterials 53 (2015) 211–220.
[27] Y. Li, L. Liu, P. Wan, Z. Zhai, Z. Mao, Z. Ouyang, D. Yu, Q. Sun, L. Tan, L. Ren, Biomaterials 106 (2016) 250–263.
[28] G. Borkow, J. Gabbay, Curr. Chem. Biol. 3 (2009) 272–278.
[29] M. Rashad, F. Pan, M. Asif, Mater. Sci. Eng. A 644 (2015) 129–136.
[30] C. Liu, X. Fu, H. Pan, P. Wan, L. Wang, L. Tan, K. Wang, Y. Zhao, K. Yang, P.K. Chu, Sci. Rep. 6 (2016) 27374.
[31] J. Zhang, Z. Leng, M. Zhang, J. Meng, R. Wu, J. Alloy. Comp. 509 (2011) 1069–1078.
[32] K. Asano, H. Enoki, E. Akiba, J. Alloy. Comp. 480 (2009) 558–563.
[33] H. Asgharzadeh, E. Yoon, H. Chae, T. Kim, J. Lee, H. Kim, J. Alloy. Comp. 586 (2014) S95–S100.
[34] M.E. Turan, Y. Sun, Y. Akgul, J. Alloy. Comp. 740 (2018) 1149–1158.
[35] E. Ghasali, M. Alizadeh, K. Shirvanimoghaddam, R. Mirzajany, M. Niazmand, A. Faeghi-Nia, T. Ebadzadeh, Mater. Chem. Phys. 212 (2018) 252–259.
[36] N.Q. Cao, D.N. Pham, N. Kai, H.V. Dinh, S. Hiromoto, E. Kobayashi, Metals 7 (2017) 358.
[37] N. Saheb, Z. Iqbal, A. Khalil, A.S. Hakeem, N. Al Aqeeli, T. Laoui, A. Al-Qutub, R. Kirchner, J. Nanomater. (2012) 18, 2012.
[38] M. Hussein, C. Suryanarayana, N. Al-Aqeeli, Mater. Des. 87 (2015) 693–700.
[39] P. Moazzen, M.R. Toroghinejad, F. Karimzadeh, J. Vleugels, H. Ravash, P. Cavaliere, Powder Metall. 61 (2018) 405–416.
[40] L. Zhang, Y. Zhang, Y. Jiang, R. Zhou, J. Alloy. Comp. 644 (2015) 513–522.
[41] Z. Ghaferi, S. Sharafi, M. Bahrololoom, Appl. Surf. Sci. 355 (2015) 766–773.
[42] A. Standard 4, American Society for Testing and Materials Annual, Philadelphia, PA, USA, 2004.
[43] H. Bakhsheshi-Rad, M. Abdul-Kadir, M. Idris, S. Farahany, Corros. Sci. 64 (2012) 184–197.
[44] S. Zhang, X. Zhang, C. Zhao, J. Li, Y. Song, C. Xie, H. Tao, Y. Zhang, Y. He, Y. Jiang, Acta Biomater. 6 (2010) 626–640.
[45] N. Golafshan, M. Kharaziha, M. Fathi, Carbon 111 (2017) 752–763.
[46] H. Arami, A. Simchi, Mater. Sci. Eng. A 464 (2007) 225–232.
[47] N. Nemati, R. Khosroshahi, M. Emamy, A. Zolriasatein, Mater. Des. 32 (2011) 3718–3729.
[48] S.N. Alam, Mater. Sci. Eng. A 433 (2006) 161–168.
[49] M. Aravind, P. Yu, M. Yau, D.H. Ng, Mater. Sci. Eng. A 380 (2004) 384–393.
[50] S. Lathabai, P. Lloyd, Acta Mater. 50 (2002) 4275–4292.
[51] T. Uesugi, K. Higashi, Comput. Mater. Sci. 67 (2013) 1–10.
[52] S. Sandlöbes, Z. Pei, M. Friák, L.-F. Zhu, F. Wang, S. Zaefferer, D. Raabe, J. Neugebauer, Acta Mater. 70 (2014) 92–104.
[53] C. Hsu, P. Kao, N. Ho, Scripta Mater. 53 (2005) 341–345.
[54] T.B. Bhat, V. Arunachalam, Proc. Indian Acad. Sci. Sect. C: Eng. Sci. 3 (1980) 275–296.
[55] S. Hassan, M. Gupta, Mater. Res. Bull. 37 (2002) 377–389.
[56] Z. Trojanova, Z. Drozd, P. Lukáč, F. Chmelik, Mater. Sci. Eng. A 410 (2005) 148–151.
[57] S. Zhang, J. Li, Y. Song, C. Zhao, X. Zhang, C. Xie, Y. Zhang, H. Tao, Y. He, Y. Jiang, Mater. Sci. Eng. C 29 (2009) 1907–1912.
[58] N.T. Kirkland, N. Birbilis, M. Staiger, Acta Biomater. 8 (2012) 925–936.
[59] M. Bornapour, N. Muja, D. Shum-Tim, M. Cerruti, M. Pekguleryuz, Acta Biomater. 9 (2013) 5319–5330.
[60] Z. Chun-Yan, Z. Rong-Chang, L. Cheng-Long, G. Jia-Cheng, Surf. Coating. Technol. 204 (2010) 3636–3640.
[61] F. Cao, G.-L. Song, A. Atrens, Corros. Sci. 111 (2016) 835–845.
[62] M. Razavi, M. Fathi, O. Savabi, S.M. Razavi, B.H. Beni, D. Vashaee, L. Tayebi, Ceram. Int. 40 (2014) 3865–3872.
[63] E. Meng, S. Guan, H. Wang, L. Wang, S. Zhu, J. Hu, C. Ren, J. Gao, Y. Feng, Appl. Surf. Sci. 257 (2011) 4811–4816.
[64] K. Cashman, A. Baker, F. Ginty, A. Flynn, J. Strain, M. Bonham, J. O'Connor, S. Bügel, B. Sandström, Eur. J. Clin. Nutr. 55 (2001) 525.
[65] N.J. Hallab, C. Vermes, C. Messina, K.A. Roebuck, T.T. Glant, J.J. Jacobs, J. Biomed. Mater. Res. 60 (2002) 420–433.
[66] E. Padan, E. Bibi, M. Ito, T.A. Krulwich, Biochim. Biophys. Acta Biomembr. 1717 (2005) 67–88.
[67] L. Ren, X. Lin, L. Tan, K. Yang, Mater. Lett. 65 (2011) 3509–3511.
[68] E.L. Yu-sen, R.D. Vidic, J.E. Stout, C.A. McCartney, L.Y. Victor, Water Res. 32 (1998) 1997–2000.